Accepted Manuscript

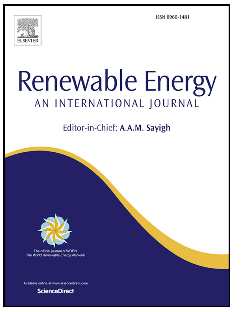

Hydro-abrasive erosion in Pelton turbine injectors: A numerical study

Gianandrea Vittorio Messa, Simone Mandelli, Stefano Malavasi

PII: S0960-1481(18)30716-X

DOI: 10.1016/j.renene.2018.06.064

Reference: RENE 10220

To appear in: *Renewable Energy*

Received Date: 29 December 2017

Revised Date: 14 June 2018

Accepted Date: 16 June 2018

Please cite this article as: Messa GV, Mandelli S, Malavasi S, Hydro-abrasive erosion in Pelton turbine injectors: A numerical study, *Renewable Energy* (2018), doi: 10.1016/j.renene.2018.06.064.

Hydro-abrasive erosion in Pelton turbine injectors: a numerical study

Gianandrea Vittorio Messa*, Simone Mandelli, Stefano Malavasi

DICA, Politecinco di Milano, Piazza Leonardo da Vinci, 32 20133 Milano, Italy

Abstract

Numerical simulations were performed to investigate how the design and the operation conditions of a Pelton turbine injector affect its vulnerability to hydro-abrasive erosion, alongside with its flow control capacity. Use was made of a Volume Of Fluid (VOF) model for simulating the free nozzle jet, a Lagrangian particle tracking model for reproducing the trajectories of the silt particles, and two erosion models for estimating the mass removal. The comparison against earlier studies and the experimental evidence, integrated with a careful sensitivity analysis, gave strength to the reliability of the numerical model. Nozzle seat and needle were the injector components most vulnerable to erosion. As the valve was closing, the erosion of the needle strongly increased, whilst that of the nozzle seat remained broadly constant. The influence of the injector design was also explored, suggesting that a reduction of the needle vertex angle is likely to enhance the risk of erosive wear. Finally, it was found that the possibility to condense the effects of the needle stroke and the needle vertex angle in a single parameter (i.e.

*Corresponding author

Email addresses: gianandreavittorio.messa@polimi.it (Gianandrea Vittorio Messa), simone.mandelli@polimi.it (Simone Mandelli), stefano.malavasi@polimi.it (Stefano Malavasi)

Preprint submitted to Renewable Energy *June 18, 2018*

the effective opening area) is no more allowed when hydro-abrasive erosion is considered, thereby assessing the need for case-specific wear prediction analyses.

Keywords: Computational fluid dynamics; discharge coefficient; hydro-abrasive erosion; Pelton turbine injector.

1. Introduction

In a Pelton turbine, the proper interaction between the water jet and the blades is fundamental for the efficiency of the device. In this context, an important role is played by the injector, which is used both for generating the high-speed jet and regulating the flow rate. Particularly, a needle valve throttles the flow in the injector, and the control of the flow is achieved by adjusting the needle stroke, s, in the nozzle. Figure 1 shows the main geometrical parameters of the needle-nozzle system, namely the constant aperture diameter of the nozzle, D_0, the needle vertex angle, γ_{n}, and the contraction angle of the nozzle seat, γ_{ns}.

When investigating the regulation characteristics of the injector, is it a common practice to make reference to the discharge coefficient, φ_{D_0}, which is defined as:

$$\varphi_{D_0} = \frac{4Q_{\mathrm{jet}}}{\pi D_0^2 \sqrt{2gH}} \tag{1}$$

where Q_{jet} is the water flow rate through the injector nozzle, g is the modulus of the gravitational acceleration, and H is the net head at the injector entrance. At a certain distance from the plane of the injector outlet, the jet has a minimum area where all the streamlines are parallel. Such narrow section was referred to as "waist section" by Zhang [1], who demonstrated that, under the assumption that the head drop in the injector is negligible compared to H, φ_{D_0} represents the ratio of the jet diameter in the waist section to the diameter of the nozzle aperture.

The trend of φ_{D_0} versus the dimensionless needle stroke, s/D_0, is usually called "injector characteristics".

A certain number of studies were reported in the literature regarding the fluid dynamic behavior of Pelton turbine injectors. With the exception of few studies entirely based on physical experiments [1–3], most investigations relied, in part or in full, on Computational Fluid Dynamics (CFD) simulations. For instance, in their upgrading and refurbishment of the injector nozzles of a Pelton turbine for the water power plant of Tillari in India, Veselý and Varner [4] assessed the effect of the design modifications on the injector characteristics via CFD and experiments on a prototype model. Koukouvinis et al. [5] proposed a numerical technique based on Smoothed Particles Hydrodynamics (SPH) as a tool for injector design based on the predicted inherent characteristic curve. Benzon et al. [6] employed two commecial CFD codes to investigate the influence of the injector geometry on its dissipation characteristics based on 2D axi-symmetric simulations, and suggested two values of γ_{n} and γ_{ns} which reduce the energy consumption required to produce a given flow rate. In a later study [7], the same researchers gave strength to the obtained results by performing more complex 3D simulations of the injector installed in Turgo and Pelton turbines. Jo et al. [8] combined CFD and laboratory tests to assess the effect of the nozzle contraction angle upon the discharge coefficient of the injector, the quality of the jet, and the overall Pelton turbine efficiency. Zeng et al. [9] numerically investigated how the fluid dynamic characteristics of the jet are affected by the elbow pipe upstream the device and the inner ribs for different needle strokes. Finally, a result of considerable impact for injector design was reported in Zhang's book [1], and it consists in the possibility to unify the influences of γ_{n} and s/D_0 on the discharge coefficient into a single parameter, called "effective opening area". This variable is defined as the ratio between the opening area, A_D, calculated as follows

$$A_D = \pi \left(1 - \frac{s}{2D_0} \sin 2\gamma_{\mathrm{n}}\right) D_0 s \sin \gamma_{\mathrm{n}} \tag{2}$$

and the nozzle area, $A_{D_0} = \pi D_0^2/4$.

In hydro turbines, the presence of solid particles carried along with the flow is a concern to engineers because, when the solids hit the turbine surface, they can produce material removal. This phenomenon, referred to as hydro-abrasive erosion, is particularly significant in some world regions where the natural water is seasonally rich in silt, which is difficult to remove [10]. The erosion by silt sediment could have negative influence on the produced power due to the decay of the efficiency and to the growth of extraordinary maintenance. In their reviews of hydro-abrasive erosion of hydraulic turbines, Padhy and Saini [11] and Felix et al. [12] listed the parts of Pelton components mainly affected by this phenomenon, namely needle tips, seat rings and injector nozzles, runner buckets, jet deflector, protection roof of injectors, casing, and grating below runner. However, the majority of the studies focused on the hydro-erosion of buckets. M.K. Padhy and R.P. Saini carried out extensive research on this topic based on experiments on a small-scale Pelton turbine. In a first work [13], they proposed an interpolatory formula for the mass loss of Pelton buckets as a function of the silt concentration, the silt size, the jet velocity, and the operating hours. Later [14], they correlated the erosion of Pelton buckets to the efficiency reduction of the turbine, and developed another empirical formula which, starting from the same input parameters, estimates directly the percentage efficiency loss. Finally [15], they discussed the main erosion mechanisms occurring at various locations of Pelton buckets for different sizes of the abrasive particles. Abgottspon et al. [16] investigated the erosion of Pelton buckets based on a case study of the Fieschertal hydropower plant, and concluded that the loss of material and the reduction in efficiency correlate only to a minor degree with the sediment load, whilst an important role is played by local conditions (such as particle properties), the design characteristics, the mode of operation, and, very important, the status of the runner at the beginning of the sediment season. A series of measurements on two Pelton turbines in the Toss hydropower plant in India, performed during the period May-October 2015, allowed Rai et al. [17] to make a detailed analysis of hydro-abrasive erosion in Pelton buckets, identifying five different erosion categories. During the same period, the authors constantly monitored the sediments entering the turbine, observing that, whilst size and concentration underwent significant variation, the shape of the grains remained substantially unchanged. In another study, Rai et al. [18] developed a simplified model for the estimation of the particle velocity and inclination angle relative to the rotating Pelton buckets, which were identified as the key parameters affecting erosion. The model was applied to a considerable number of real-case scenarios, leading to recommendations for the design and operation of Pelton turbines in order to reduce their vulnerability to hydro-abrasive wear. A similar approach was followed by Zhang [1], who derived a simplified model to numerically track the particle motion in the water-sheet flow within the Pelton buckets.

Fewer papers specifically concerned the hydro-abrasive erosion of the Pelton injectors. Bajracharya et al. [10] investigated the erosion of the needles of the Pelton turbines installed in the Chilime hydroelectric plant in Nepal, reporting some photographs and wear profiles. The authors estimated the penetration rate (that is, the rate at which the erosion depth increases) and the efficiency reduction experienced by the turbines, and they suggested an interpretation of the needle erosion based on fluid dynamic considerations. The particularly severe erosion of the needle was ascribed to the combined effects of hydro-abrasive erosion and cavitation, which were supposed to be enhanced when the injector operated in partial opening condition. Evidence of the synergistic effect of the two phenomena in Pelton needle had been previously reported also by Thapa et al. [19] and discussed in the review paper by Gohil and Saini [20]. Recently, Morales et al. [21] estimated the erosion behavior of the needle at Chivor hydroelectric plant in Colombia by measuring the evolution of its surface roughness, and developed a setup to reproduce the phenomenon at the laboratory scale. The authors found that, after an incubation period, a fast increase in roughness occurred, and the enhancement in the mass removal was attributed to the fact that the hydro-abrasive erosion promoted the onset of cavitation erosion.

Nowadays, CFD has high potential for the analysis of critical working conditions in hydraulic machinery such as turbines and pumps, including cavitation, solid particle erosion, and flow-induced noise (e.g. [22–24]). The numerical approach, in fact, allows attaining detailed information and it is substantially free from several difficulties inherent in experimental and field testing. Particularly, a well established methodology is available for CFD-based wear estimation, and it consists of two steps in sequence [25]. First, the fluid-particle flow field is simulated by means an Eulerian-Lagrangian two-phase model [26], in which the fluid flow is represented in an Eulerian, cell-based framework, whilst the solid phase is represented in a Lagrangian framework by following the trajectories of a certain number of particles. Afterwards, a single-particle erosion model is applied to estimate the loss of material produced by each particle-wall collision and, in turn, the overall erosion of the walls.

A single-particle erosion model is an algebraic equation relating the erosion ratio of a particle-wall collision, $E_{\rm coll}$ (i.e. the ratio between the mass of material removed, $W_{\rm p}$, and the mass of the particle, $m_{\rm p}$) as a function of several parameters, including the modulus of the particle velocity at the impact stage, $|\boldsymbol{v}_{\rm p,imp}|$, the particle impingement angle, $\theta_{\rm p,imp}$, some particles-related quantities, such as its shape and size, and some mechanical properties of the target material, such as its hardness (Fig. 2). The effectiveness of single-particle erosion models arises from their capability to correctly capture the physical processes associated with material removal. In the case of ductile materials, the existence of two erosion mechanisms has been established since pioneering works such as Bitter [27], where they were called cutting wear and deformation wear. Cutting wear mainly occurs at low impact angles, and it is associated with a shearing action. Deformation wear is characteristic of high impact angles and, even if the basic physical process was not agreed upon by researchers [28], an interpretation still shared attributes the mass removal to repeated particle impacts causing plastic deformation, hardening, and sub-surface cracking [29].

Several researchers, including Bitter [27, 30], Neilson and Gilchrist [31], Grant and Tabakoff [28], Huang et al. [32], and Arabnejad et al. [29, 33], proposed phenomenological erosion models that quantify the contributions from cutting and deformation wear separately. These models provide intuitive appreciation of the physical phenomena underlying erosion. At the same time, the wear estimates appear sensitive on several material- or particle-related parameters which are very difficult to quantify, and are usually calibrated from laboratory experiments in which a high-velocity particle-laden jet impinges against a specimen at a certain inclination angle (Fig. 3). In these tests, the carrier fluid is typically air, so that the particles follow straight lines and the particle impact angle is approximately equal to the nozzle-to-specimen angle. Conversely, the particle impact velocities are likely to be lower than the air jet velocity at the nozzle exit, and are generally estimated by image techniques or CFD simulations.

Other erosion models can be classified as empirical, in the sense that they were directly obtained by fitting the outcomes of the experimental tests sketched in Fig. 3 and do not have a rigorous physical derivation. It is noted that, generally, the form of the mathematical expressions to be calibrated arises from physical considerations, thereby making the boundary between phenomenological and empirical erosion models not easily drawn. A common feature of empirical erosion models is that the tuning constants are not given a precise physical characterization, but express general concepts such as particle or material property. The wide applicability of empirical erosion models, even in an engineering context, comes from the fact that, typically, the predictive equations can be utilized for many materials and any impact condition. On the other side, they allow limited understanding of the material behavior itself. The models which will be employed in this study, presented later in section 2.3, belong to the category of empirical erosion models.

For the sake of completeness, it is noted that alternatives to the traditional single-particle erosion models have been reported in the literature. Lyczkowski and Bouillard [34] discussed power and energy dissipation erosion models, which interpret erosion as a result of the energy transferred from the solids to the eroding surfaces. Recently, Leguizamón et al. [35] developed a multiscale model which relies on the simulation of the sediment impact process at the sub-particle scale. Finally, some new modeling approaches were proposed by the authors of this paper to increase the applicability of CFD-based wear estimation methods [36–38].

Apart from these innovative efforts, the standard CFD-based methodology previously described has been often applied to different types of turbines, and the focus was usually on the erosion of the blades [39–48]. However, in the extensive literature review carried out in this study, the authors did not find any publication regarding the numerical investigation of the impact erosion in Pelton turbine injectors other than a couple of papers by Zeng et al. [49, 50]. In [50], the flow field of the free jet produced by the injector was analyzed, the trajectories of 50 μm size particles were tracked, and an empirical erosion model was used to identify the areas of the needle-nozzle system most exposed to erosion. Following the same approach, the effect of particle size was briefly explored in a previous publication of the same researchers [49].

Purpose of the present paper was to contribute to the knowledge of hydro-abrasive erosion in Pelton turbine injectors, and, particularly, the main focus was on the use of the injector as flow control device. A systematic CFD study was carried out to predict the loss of material caused by the impingements of silt particles carried along with the flow over the entire travel rate of the needle and for three different needle vertex angles, $\gamma_{\rm n}$, in order to establish the influence of these geometrical and operation parameters on the erosion characteristics of the device. The numerical results, discussed on the basis of the physical processes underlying particle transport and hydro-abrasive erosion, showed consistency with earlier studies and the experimental evidence. The remainder of the paper is divided in three sections, followed by the conclusions. In section 2, details on the mathematical model and the solution algorithm are provided. In section 3, the key simulation parameters are reported, and the consistency and the reliability of the numerical solution are assessed. Finally, in section 4, the obtained results are illustrated and discussed.

2. Mathematical model

The modeling approach used in the present study was analogous to that of Zeng et al. [49, 50], except for the fact that a specific analysis of the influence of the erosion model was here performed. The low mass loading considered in the simulations (1‰), consistent with the values recorded during flood events [10], enabled the hypothesis of one-way coupling regime, i.e. the assumption that the fluid flow is not affected by the presence of the particles [51]. This allowed decoupling the determination of the regulation characteristics of the injector and the estimation of wear due to silt particles. A Volume Of Fluid (VOF) multiphase model was employed to reproduce the free water jet leaving the injector, in order to provide a fluid-dynamic characterization of the device. The calculation of the particle trajectories was then performed over the VOF predictions and, finally, single-particle erosion models were employed to obtain the wear estimates.

2.1. The VOF model for the fluid-dynamic characterization of the injector

The free water jet in air produced by the injector was simulated by means of the VOF multiphase model under steady-state flow conditions and treating both phases as incompressible. No phase change was assumed for the water phase and, therefore, the possible presence of cavitation regions was not accounted for. In the VOF model, the water-air mixture is considered as a single fluid with properties depending on the local volume fractions of the two phases, namely:

$$\psi = \psi_{\mathrm{w}}\alpha_{\mathrm{w}} + \psi_{\mathrm{a}}\alpha_{\mathrm{a}} \tag{3}$$

where ψ_w, ψ_a, and ψ are generic fluid dynamic properties (i.e. density, ρ, and viscosity, μ) of the water phase, the air phase, and the water-air mixture, respectively; α_w and α_a are the volume fractions of the water and air phases, respectively. Reynolds averaged formulations of the fundamental conservation equations were solved. The mass conservation equation for the mixture is

$$\nabla \cdot (\rho \boldsymbol{U}) = 0 \tag{4}$$

where $\boldsymbol{U}$ is the mean velocity vector of the mixture. The momentum conservation equation for the mixture with the Boussinesq assumption is

$$\nabla \cdot (\rho \boldsymbol{U}\boldsymbol{U}) = -\nabla P + \nabla \cdot \left[(\mu + \mu_\mathrm{t}) \left(\nabla \boldsymbol{U} + \nabla \boldsymbol{U}^T \right) \right] + \rho \boldsymbol{g} \tag{5}$$

where P is the mean pressure of the mixture, μ_t is the eddy viscosity, and $\boldsymbol{g}$ is the gravitational acceleration vector. Finally, in the VOF model, the tracking of the interface between the gas and the liquid is accomplished by the solution of a continuity equation for the gas volume fraction, which, under the assumptions made (i.e. steady-state, incompressible two-phase flow without mass exchanges between air and water), reduces to:

$$\nabla \cdot (\alpha_\mathrm{a} \boldsymbol{U}) = 0 \tag{6}$$

The volume fraction equation for the water phase was not solved explicitly, but α_w was obtained by the constrain

$$\alpha_\mathrm{a} + \alpha_\mathrm{w} = 1 \tag{7}$$

At the interface, identified by those cells in which $0 < \alpha_\mathrm{w} < 1$, a force due to the surface tension coefficient, $\boldsymbol{F}_\sigma$, was added as a source term in the momentum equation for the mixture (Eq. 5). $\boldsymbol{F}_\sigma$ is given by

$$\boldsymbol{F}_\sigma = \sigma \kappa \nabla \alpha_\mathrm{w} \tag{8}$$

where σ is the surface tension coefficient and κ is the surface curvature, namely:

$$\kappa = \nabla \cdot \frac{\nabla \alpha_{\mathrm{w}}}{|\nabla \alpha_{\mathrm{w}}|} \tag{9}$$

The eddy viscosity, μ_{t}, was evaluated by means of the realizable $k - \varepsilon$ turbulence model [52].

2.2. The Lagrangian particle tracking model

As already mentioned, owing to the "one-way coupling" regime assumption, the Lagrangian tracking calculations were performed after the VOF simulation. Following a common practice in particle tracking in order to keep the computational load within reasonable limits, the "parcel" approach was adopted. As well documented in Crowe et al. [26], this approach relies on the identification of groups of particles with identical characteristics (size, shape, density, velocity, and position). Such groups are called "parcels" and, hereafter, will be denoted by the subscript P, whereas the term "particle" and the subscript p will indicate the physical grain. Trajectories were calculated for all parcels by solving the following ordinary differential equations:

$$\frac{d\boldsymbol{x}_{\mathrm{P}}}{dt} = \boldsymbol{v}_{\mathrm{P}} \tag{10a}$$

$$\frac{d\boldsymbol{v}_{\mathrm{P}}}{dt} = \frac{3}{4d_{\mathrm{p}}} \frac{\rho}{\rho_{\mathrm{p}}} C_{\mathrm{d}} |\boldsymbol{u}_{@\mathrm{P}} - \boldsymbol{v}_{\mathrm{P}}| \left(\boldsymbol{u}_{@\mathrm{P}} - \boldsymbol{v}_{\mathrm{P}}\right) + \frac{1}{\rho_{\mathrm{p}}} \nabla P_{@\mathrm{P}} \tag{10b}$$

where: t is the Lagrangian calculation time; $\boldsymbol{x}_{\mathrm{P}}$ and $\boldsymbol{v}_{\mathrm{P}}$ are the instantaneous position and velocity vectors of the current parcel, respectively; d_{p}, ρ_{p}, and C_{d} are the size, the density, and the drag coefficient of the particles in the current parcel, respectively; and the "@P" subscript indicates that the instantaneous velocity vector of the water-air mixture, $\boldsymbol{u}$, and the gradient of the mean pressure, ∇P, are evaluated at parcel position. The drag coefficient was estimated by the correlation of Schiller and Naumann [53] for spherical particles:

$$C_\mathrm{d} = \begin{cases} \dfrac{24}{Re_\mathrm{p}} \left(1 + 0.15 Re_\mathrm{p}^{0.687}\right), & \text{if } Re_\mathrm{p} \leq 1000 \\ 0.44, & \text{otherwise} \end{cases} \tag{11}$$

where $Re_\mathrm{p} = \rho d_\mathrm{p} |\boldsymbol{u}_{@\mathrm{P}} - \boldsymbol{v}_\mathrm{P}| / \mu$ is the particle Reynolds number.

Other forces, such as gravity, lift, added mass, and history force, were neglected because previous studies [36] and theoretical considerations [51] suggested their minor importance for the flows addressed in this study. The instantaneous velocity vector of the fluid, $\boldsymbol{u}$, was obtained by a standard, well-established "discrete random walk" stochastic model embedded in the used CFD code [54].

The Lagrangian tracking problem was solved as steady-state and, therefore, each parcel was attributed a fixed mass flux, $\dot{m}_\mathrm{P}$, which remained constant along its trajectory.

2.3. Erosion models

The significant role played by the erosion model in affecting the wear estimates, assessed by two authors of this paper in previous studies [36, 55], led to the decision of employing two different equations, in order to test the robustness of the simulation results. The two correlations were selected among those available in the literature [25, 34] mainly because of the wide applicability, the widespread diffusion, and the easiness of use in terms of number and types of input parameters. Both models can be regarded as mostly empirical and, therefore, they were substantially obtained from calibration of laboratory experiments without a strong theoretical foundation.

The first model employed was that developed by Oka and co-workers, whose final formulation, reported in [56, 57], required years of work and several intermediate steps [58, 59]. According to this model, which will be referred to as "Oka" in the remainder of the paper, the erosion (mass) ratio of a particle-wall collision, E_{coll}, is given by:

$$E_{\mathrm{coll}} = 10^{-9}\rho_{\mathrm{t}} K \left(aH_{\nu}\right)^{k_1 b} \left(\frac{|\boldsymbol{v}_{\mathrm{p,imp}}|}{V'}\right)^{k_2} \left(\frac{d_{\mathrm{p}}}{D'}\right)^{k_3} f\left(\theta_{\mathrm{p,imp}}\right) \quad (12a)$$

$$f\left(\theta_{\mathrm{p,imp}}\right) = \left(\sin\theta_{\mathrm{p,imp}}\right)^{n_1}\left[1 + H_{\nu}\left(1-\sin\theta_{\mathrm{p,imp}}\right)^{n_2}\right] \quad (12b)$$

where: ρ_t and H_ν are the density and the Vickers hardness number of the target material, respectively; V' and D' are a reference velocity and a reference particle size, respectively; K is a particle property factor depending on particle shape and hardness; a and b are parameters related to the material of the eroding surface; k_1, k_2, k_3, n_1, and n_2 depend on the properties of both particles and target. The Oka correlation was obtained by fitting the data of air-solid abrasive jet impingement tests (Fig. 3) in the following conditions: impact velocities from 50 to 167 m/s; nozzle-to-specimen angles from 5° to 90°; SiO_2, SiC, and glass as particle materials; particle sizes from 49 to 428 μm; different metals as target materials with ρ_{t} from 2700 to 9020 kg/m^3 and H_ν from 0.40 to 8.00 GPa. However, it is noted that, despite its empirical nature, the model was developed starting from recognizing erosion as a combination of repeated deformation and cutting, which are associated with the two multiplied terms in Eq. 12b. In this work, the suggested parameters for SiO_2 particles were adopted, namely K=65, k_1=-0.12, k_2=$2.3H_\nu^{0.038}$, k_3=0.19, n_1=$0.71H_\nu^{0.14}$, and n_2=$2.4H_\nu^{-0.94}$. The values of the reference variables V' and D' were those considered by the experimenters when fitting their correlation, namely 104 m/s and 326 μm, respectively. Finally, a and

b characterize the load relaxation ratio of the target material, and they should be determined by ad-hoc experiments. In the lack of any indication, both parameters were taken to be unity, as commonly assumed in previous studies [60–63].

The second erosion model used in the present study was that reported in a recommended practice by Det Norske Veritas [64], and it will be called "DNV" from this point onward. The DNV model is one of the most widely used in the oil and gas industry, and it has an extremely simple formulation. The formula for E_{coll} is

$$E_{\text{coll}} = K|\boldsymbol{v}_{\text{p,imp}}|^n f\left(\theta_{\text{p,imp}}\right) \tag{13a}$$

$$f\left(\theta_{\text{p,imp}}\right) = \sum_{j=1}^{8} A_j \theta_{\text{p,imp}}^j \tag{13b}$$

where the suggested constants for steel grades are $K = 2 \cdot 10^{-9}$, $n = 2.6$, $A_1 = 9.37$, $A_2 = -42.295$, $A_3 = 110.864$, $A_4 = -175.804$, $A_5 = 170.138$, $A_6 = -98.398$, $A_7 = 31.211$, and $A_8 = -4.17$. As detailed in Haugen et al. [65], this formula was empirically obtained through abrasive jet experimentation (Fig. 3) with angular sand particles of diameter 200–250 μm, impact velocities from 18 to 220 m/s, and nozzle-to-specimen angles between 15 and 90°. Six standard steel materials were tested with density around 8000 kg/m^3 and Vickers numbers between 2.35 and 14.7.

The flow conditions addressed in the current investigation were generally within the range for which the Oka model was calibrated, except for the impact velocity, which was sometimes smaller in the numerical simulations. Conversely, the simulated particle size and the Vickers number of the target material were smaller than in experiments of Haugen et al. [65]. It is noted that, however, a number of studies demonstrated that both models can perform well outside their calibration range, even in closer flow conditions to those addressed here (e.g. [63, 66]). This consideration, in addition to those made at the beginning of this section, contributed to the choice of the erosion models to be tested.

2.4. Computational domain and boundary conditions

Half of the computational domain is shown in Fig. 4 together with the imposed boundary conditions. A stagnation inlet condition was imposed upstream the device, in which the pressure was set to a fixed value (specified later) and α_{a} was 0. Position and velocity were specified for all parcels at this boundary, where no mean relative velocity was assumed between water and solids. The initial parcels' velocities, $\boldsymbol{v}_{\mathrm{P}}^{0}$, were thus equal to the unhindered water velocities, $\boldsymbol{U}_{@\mathrm{P}}$, plus a fluctuation, as follows

$$\boldsymbol{v}_{\mathrm{P}}^{0} = \boldsymbol{U}_{@\mathrm{P}} + \boldsymbol{\xi}\sqrt{\frac{2k_{@\mathrm{P}}}{3}} \tag{14}$$

where $\boldsymbol{\xi}$ is a three-element vector containing random scalars drawn from the standard PDF, and $k_{@\mathrm{P}}$ is the unhindered turbulent kinetic energy of the fluid at parcel position. The initial parcels' positions were determined by imposing the local parcel number density to be proportional to the local advective water mass flux per unit area, i.e. $\rho_{\mathrm{w}}\left(\boldsymbol{U}_{@\mathrm{P}} \cdot \boldsymbol{n}_{@\mathrm{P}}\right)$, where $\boldsymbol{n}_{@\mathrm{P}}$ is the unit normal vector at parcel position. The total solid mass flow rate through the inlet section, $\dot{M}_{\mathrm{s}}$, was determined in such a way to produce a solid volume fraction, C, equal to 1‰, through the following formula:

$$\dot{M}_{\mathrm{s}} = \rho_{\mathrm{p}}\frac{Q_{\mathrm{jet}}}{\dfrac{1}{C} - 1} \approx \rho_{\mathrm{p}} C Q_{\mathrm{jet}} \tag{15}$$

where the volume flow rate of the water jet, Q_{jet}, was obtained as output of the VOF simulation. All parcels, whose total number is referred to as N_{P}, were attributed the same mass flux, equal to

$$\dot{m}_{\mathrm{P}} = \frac{\dot{M}_{\mathrm{s}}}{N_{\mathrm{P}}} \tag{16}$$

A stagnation inlet with total pressure of 0 bar and $\alpha_{\mathrm{a}} = 1$ was imposed laterally to the nozzle exit, and a pressure outlet condition with total pressure of 0 bar and unit backflow air volume fraction was set on all other faces of the outlet cylinder. The parcels were allowed to leave the domain through the whole outlet cylinder.

All other boundaries were solid walls. The wall treatment used in this study was two-layer all y^+, which smoothly blends the wall laws to estimate the wall shear stress and the value of the turbulence quantities in the near-wall cells [54]. Each time a parcel collided against a wall, the normal and tangential rebound velocity components were related to the corresponding incident values via two restitution coefficients. The correlations of Grant and Tabakoff [67] were briefly explored but, finally, both restitution coefficients were set to a unit value, after discovering the minor influence of these parameters upon the quantities of interest for this study.

2.5. Computational methodology

The simulations were performed employing the general-purpose, commercial CFD code STAR CCM+ version 11.02 in conjunction with in-house MATLAB routines for the definition of the parcels' initial conditions. The VOF equations, discretized via the finite volume method, were solved in a segregated manner by the STAR segregated flow model. Use was made of a second-order upwind scheme for the convective terms, a second-order central difference scheme for the diffusion terms, and a Hybrid Gauss-LSQ method for the pressure gradient. The integration of the parcel equation of motion was done by the Lagrangian steady solver with the default numerical settings [54].

By employing a specific utility available in STAR CCM+, the erosion rate intensity of each surface element (i.e. the mass of wall material eroded per unit area per unit time, referred to as Φ_{el}) was calculated, as follows

$$\Phi_{\mathrm{el}} = \frac{1}{A_{\mathrm{el}}} \sum_{i(\mathrm{el})} \dot{m}_{\mathrm{P}} E_{\mathrm{coll},i} \tag{17}$$

where A_{el} is the area of the surface element, and $i\,(\mathrm{el})$-s stand for the parcels which impinge against the surface element. In this study, $E_{\mathrm{coll},i}$ was evaluated by applying either of the two erosion models reported in section 2.3, in which $\boldsymbol{v}_{\mathrm{p,imp}}$ and $\theta_{\mathrm{p,imp}}$ were replaced by the parcels' fluid dynamic characteristics at the impingement stage. The integral erosion ratio, E_{int}, of the needle and the nozzle was computed by summing up the $A_{\mathrm{el}}\Phi_{\mathrm{el}}$ products over the surface elements of these components, and dividing by the total solid mass flux through the inflow section, $\dot{M}_{\mathrm{s}}$.

3. Problem statement and numerical parameters

3.1. Definition of the simulation scenarios

Several simulations were carried out on the injector qualitatively sketched in Fig. 1 for three needle vertex angles ($25°$, $27.5°$, and $30°$). The device was equipped with three equally spaced ribs to lead and center the needle. The nozzle diameter, D_0, was 50 mm and the nozzle contraction angle, γ_{ns}, was $40°$. For each trim, the discharge coefficient and the erosion characteristics were estimated over four values of s/D_0. The pressure upstream the injector was 40 bar, corresponding to a net heat, H, of about 410 m. The physical properties of water and air, i.e. density (ρ), viscosity (μ), and surface tension coefficient (σ), were set as the characteristic values at a temperature of 20°C, namely $\rho_{\mathrm{w}} = 998.23\ \mathrm{kg/m^3}$, $\rho_{\mathrm{a}} = 1.2041\ \mathrm{kg/m^3}$,

$\mu_{\rm w} = 1.0016 \cdot 10^{-3}$ Pa·s, $\mu_{\rm a} = 1.8205 \cdot 10^{-5}$ Pa·s, and $\sigma = 72.86 \cdot 10^{-3}$ N/m. Finally, in order to enhance the engineering relevance of this study, the mass flux of each parcel ($\dot{m}_{\rm P}$), the particle density ($\rho_{\rm p}$), and the particle size ($d_{\rm p}$) were defined in analogy with the application case analyzed by Bajracharya et al. [10]. In detail, $\dot{m}_{\rm p}$ was imposed in such a way to produce a volumetric concentration of 1‰ at the nozzle entrance (Eqs. 15 and 16) and the particles were assumed monodisperse with $\rho_{\rm p} = 2650~{\rm kg/m^3}$ and $d_{\rm p} = 50~\mu$m, representative of silt. The solids were implicitly assumed spherical in shape, as implied by the use of the Schiller and Naumann correlation for the drag coefficient (Eq. 11). The properties of the target material were chosen among the typical values reported in the literature for steels, namely $\rho_{\rm t} = 7900~{\rm kg/m^3}$ and $H_\nu = 1.34$.

3.2. Numerical consistency of the CFD solution

The consistency of the numerical solution was investigated, making reference to the minimum simulated dimensionless needle stroke for the $\gamma_{\rm n} = 27.5°$ case, which is $s/D_0 = 0.067$. This condition was chosen because the high velocity and pressure gradient in the nozzle, resulting from the small area of the exit section, were expected to enhance the effect of numerical parameters, such as the number of grid elements and the number of injected parcels.

First, the sensitivity of the discharge coefficient predictions upon the spatial discretization was investigated. Computational meshes was generated after dividing the domain in three zones, corresponding to the upstream pipe, the actual injector, and the environment downstream of the nozzle exit (Fig. 5a). Three different unstructured hexahedral meshes were employed, consisting of about 0.9, 1.7, and 3.4 million cells, and referred to as M1, M2, and M3, respectively. The number of cells (total and in each zone) is summarized for all meshes in Table 1.

The cells were densified within the nozzle and, above all, close to the needle tip and in correspondence to the air-water interface (Fig. 5b), as these are the areas where high mesh refinement is required to obtain consistent solutions. The discretization error was computed using the GCI (Grid Converge Index) method, following the procedure that Celik et al. [68] proposed on the grounds of the previous study by Roache [69]. The predicted values of ϕ_{D_0} on the three grids are reported in Table 2 together with the grid refinement factor, the extrapolated value, and the GCI on the two finer meshes. The numerical uncertainty on the fine grid solution was only 0.27% and, consequently, mesh M3 was considered adequate.

Afterwards, the consistency of the erosion estimates was analyzed, and the target parameter was the integral erosion ratio of the nozzle seat, $E_{\mathrm{int,ns}}$, estimated by the Oka erosion model (Eq. 12). In addition to the sensitivity analysis with respect to the computational mesh, the effect of the number of tracked parcels had to be assessed. In fact, since a parcel represents a group of physical particles, it was necessary to ensure that a statistically significant number of parcels were tracked, even more so because the trajectories were random due to the effect of turbulent dispersion. This was achieved by increasing the number of parcels, N_{P}, unless $E_{\mathrm{int,ns}}$ reached a stable value. Note that increasing N_{P} corresponds to decreasing the mass flux that each parcel represents (Eq. 16), and that the higher the number of parcels the lower the number of particles each parcel contains. Following a previous work [55], the combined effect of the number of grid elements and N_{P} was taken into consideration. In order to ensure further reliability of the estimates, a ten million element mesh was defined in addition to the already mentioned M1, M2, and M3. Such grid is referred to as M4 in Table 1. For each level of discretization, the number of injected parcels was increased from 5000 to 100000.

Figure 6 confirms the consistency of the wear predictions obtained using the M3 cells mesh with $N_{\mathrm{P}} = 75000$, since further increase in either the number of grid elements or the number of computed trajectories did not produce significant changes to $E_{\mathrm{int,ns}}$. Such number of parcels was considered for all combinations of γ_{n} and s/D_0. Note that, because of the changes in their geometry, the injectors produce different jet flow rates for the same H and, therefore, $\dot{M}_{\mathrm{s}}$ and $\dot{m}_{\mathrm{P}}$ are not equal for all test cases (Eqs. 15 and 16).

3.3. Assessment of the physical consistency of the VOF solution and validation

The next step in the assessment of the reliability of the CFD estimates was the verification of the physical consistency of the VOF solution and its comparison against earlier results from the literature. The typically obtained air-water flow field was that depicted in Fig. 7 for $\gamma_{\mathrm{n}} = 27.5°$ and $s/D_0 = 0.459$. As expected, the pressure dropped off towards the end of the injector, creating a flow that escaped in the form of a free jet. The jet spreading was actually negligible within the short simulated distance.

The estimated injector characteristics for the three values of γ_{n} are depicted in Fig. 8a. The numerical results were in good agreement with the curves reported in Zhang's book [1]. Unfortunately, the experiments from which these curves were obtained were described in an earlier report not accessible to the public and, therefore, the geometrical details and the testing conditions were substantially unknown. Nevertheless, it is noted that all the data series collapsed into a single one if s/D_0 was replaced by the effective nozzle opening area, A_D/A_{D_0}, and, furthermore, the resulting curve largely overlapped the experimental results (Fig. 8b). This lent confidence to the air-water flow model and, at the same time, it confirmed Zhang's claim that it is possible to estimate a priori the injector characteristics for a given

γ_n if the curve corresponding to another γ_n is known.

The reliability of the erosion predictions will be a subject of discussion in the following section.

4. Results and discussion

4.1. Particle tracking and typical wear predictions

After computing the air-water flow field, the trajectories of 75000 parcels were tracked. As an example, Fig. 9a displays the paths followed by 15 representative parcels as they move through the injector, colored by their local velocity magnitude, for $\gamma_n = 27.5°$ and $s/D_0 = 0.459$. The parcels tend to move parallel to the nozzle casing, flowing around the supporting ribs. As they reach the contraction nozzle, they undergo sudden acceleration, increasing their velocity up to about 80 m/s and, eventually, collide with the surfaces of the nozzle and the needle. From a qualitative point of view, the obtained results are very similar to those of the earlier simulations of Zeng et al. [50]. Figure 9b allows further exploring the fluid dynamic behavior of the solids by showing the same trajectories colored by their local Stokes number in logarithmic scale. The Stokes number is defined as:

$$St_\Lambda = \frac{\tau_p}{\tau_\Lambda} \tag{18}$$

where τ_p is the particle response time, which expresses the responsiveness of a particle to a change in the fluid velocity, and τ_Λ us a characteristic fluid time scale. The Stokes number is a measure of the temporal correlation between the particle velocity and the fluid velocity field. Particles with $St_\Lambda \ll 1$ tend to follow the fluid streamlines, behaving as a passive scalar, whereas those having $St_\Lambda \geq 1$ will not be able to follow rapid changes in the fluid streamline [26, 51]. The Stokes number acquires particular importance in relation to impact erosion because, in order to collide against a surface, a particle must necessarily detach from a fluid streamline. Thus, having local St_Λ not much smaller than one is a necessary condition for particle-wall impingements to occur, whilst the impact velocity and the impact angle affect the damage that a colliding particle can produce. τ_p and τ_Λ were calculated along the parcels' trajectories by means of the following formulas:

$$\tau_\mathrm{p} = \frac{4}{3}\frac{\rho_\mathrm{p} d_\mathrm{p}}{\rho C_\mathrm{d} |\boldsymbol{u}_{@\mathrm{P}} - \boldsymbol{v}_\mathrm{P}|} \tag{19}$$

$$\tau_\Lambda = C_L \frac{k_{@\mathrm{P}}}{\varepsilon_{@\mathrm{P}}} \tag{20}$$

in which $C_L = 0.15$, as this is the typical time constant in the k-ε framework. Inspection of Fig. 9b reveals that, owing to the small value of particle size, the parcels substantially followed the fluid in the inlet tube ($St_\Lambda \approx$ 0.10), whilst St_Λ becomes higher close to the contraction nozzle, exceeding 10 in proximity of the nozzle outlet edge. This result had a clear correspondence with the locations of particle-wall impingements, which were densified in the end part of the injector, as shown in Fig. 9c based on a sample of 5000 parcels. The points in Fig. 9c are colored by the impact velocity magnitude, which assumed the maximum values at the outlet edge of the nozzle seat. Thus, the greatest erosion damage could be expected at this location.

And indeed, when the Oka erosion model (Eq. 12) was employed to estimate the local erosion rate intensity of the surface elements on the inner walls of the injector, the end of the nozzle seat was found to be the part of the device most subjected to wear (Fig. 10a), even if some damage was found also on the needle (Fig. 10b). Similar results, although at a lower resolution, were found by Zeng et al. [50].

4.2. *Effect of the injector opening on erosion*

Figure 11a depicts the integral erosion ratio of the nozzle seat and the needle as a function of the dimensionless needle stroke, s/D_0, for $\gamma_{\rm n} = 27.5°$. Particularly, the estimates of the Oka and the DNV erosion models have been compared. As already observed for other types of flows [36, 55, 66], also in this case the use of different erosion correlations produced significant variations in the wear predictions. However, the erosion model had practically no effect on the qualitative behavior of the s/D_0-$E_{\rm int}$ curves. With both options, the integral erosion ratio of the nozzle seat was higher compared to that of the needle, and the difference tended to disappear as s/D_0 is reduced. Similar relative weights of the two contributions were predicted by Zeng et al. [50]. The photographs reported by Bajracharya et al. [10] and Neopane et al. [70] may suggest that the CFD model was capable in correctly predicting the location of erosion but, at the same time, the erosion of the needle was likely to be underestimated. A plausible interpretation could be that the actual needle wear is enhanced by the already mentioned coalesced effect of cavitation and impact erosion [10, 19, 20], a feature that was not accounted for in the numerical simulations.

At present, the absence of reproducible experimental data does not allow assessing which of the two erosion models provides more accurate mass loss predictions. In an earlier investigation [55], two authors of this paper found that the Oka model procured the overall best agreement with experimental data for slurry abrasive jet impingement tests, whereas the DNV model tended to underestimate the mass removals. Furthermore, the Oka model accounts for the effect of more variables (i.e. particle size and material hardness) and its calibration range is closer to the flow conditions addressed in this study. All these considerations may suggest that, compared to the DNV one, the Oka model procures more reliable estimates but, without an experimental validation, it is not possible to reach definitive conclusions. On the other side, it was interestingly noted that, if the E_{int} values were divided by a reference quantity, E^* (here taken as the integral erosion ratio of the nozzle for $s/D_0 = 0.45$), the dependence upon the erosion model could be substantially eliminated without affecting the relative weights of wear on the two components of the injector (Fig. 11b). This finding is relevant for the applications. In fact, often, the scope of the engineering simulation is not to accurately estimate the entity of hydro-abrasive erosion, but, rather, to allow reliable comparisons of different scenarios, and it is here proven that this can be achieved by referring to E_{int}/E^* instead of E_{int}.

The trend of the integral erosion ratio versus the needle stroke had a clear correspondence with the distribution of erosion rate intensity, which is depicted in the third columns of Figs. 12 and 13 for the nozzle seat and the needle, respectively. In fact, whilst the wear of the nozzle seat was almost constant with s/D_0, and confined along the outlet lip, the material removal from the needle nose considerably increased as the valve was closing. In order to further investigate this behavior, attention was turned to the most basic fluid-dynamic parameter affecting erosion, namely number of impingements, modulus of the impact velocity, and impact angle. These can be inspected in the first two columns of Figs. 12 and 13, obtained by sampling the computed parcels' characteristics at the impingement stage. The variation of s/D_0 did not result in appreciable changes in the number of impingements on the inner wall of the nozzle seat, and the combination of either low impact velocity or low impact angle resulted in negligible wear except close to the exit edge. Conversely, the increase in the erosion of the needle at low

s/D_0 could be explained by the higher number of impacts and the higher impact velocities. Finally, it is noted that the impact angles were generally lower than $20°$ on both the nozzle seat and the needle, thereby suggesting that cutting is likely to be the dominant erosion mechanism in Pelton turbine injectors.

4.3. Effect of the needle vertex angle on erosion

Finally, the influence of the needle vertex angle, $\gamma_{\rm n}$, on erosion was studied for the whole range of needle strokes. In order to reduce the influence of the erosion model, the integral erosion ratio was divided by that of the needle at $s/D_0 = 0.45$ and $\gamma_{\rm n} = 27.5°$. The results, shown in Fig. 14a, indicated that, within the range considered, the needle vertex angle did not affect the qualitative behavior of the wear curves and the relative weights of the erosion of the needle and the nozzle seat. Nevertheless, erosion seemed more pronounced for low values of $\gamma_{\rm n}$, this trend being more evident for the needle. Providing a rigorous justification of this result was definitely hard due to complexity of the computational model and the number of concurrent physical mechanisms involved, but some interpretation could be argued with the help of the sketch in Fig. 15, which depicts a typical parcel trajectory in the space between the needle and the nozzle seat. For both components, an increase in $\gamma_{\rm n}$ contribute to a reduction of the impingement angles, referred to as β_i in the sketch, and, at the same time, an increase in the distance between two consecutive impingements. Since the low β_i values (below $20°$, see also Figs. 12 and 13) belong to the range in which the impact angle function is monotonically increasing, both variations cause a reduction of erosion. Finally, it is noted that, unlike the discharge coefficient, the erosion curves did not collapse when plotted as a function of the effective opening area (Fig. 14b), underlining that the fluid dynamic similarity condition guessed by Zhang for the discharge coefficient [1] did not extend to the loss of material arising from the presence of solid particles in the flow.

5. Conclusions

In this paper, the problem of hydro-abrasive erosion in Pelton turbine injectors was investigated by means of numerical simulations. The main innovative aspect is that, for the first time, a systematic analysis of the wear characteristics of the injector was carried out by focusing on its use as a flow control device. A Volume Of Fluid (VOF) model was employed to reproduce the water flow inside the injector and the free jet, and a Lagrangian particle tracking model was used in conjunction with two erosion correlations to estimate the loss of material caused by the impingements of silt particles within the fluid. The reliability of the numerical model was guaranteed by a consistency analysis followed by a two-step validation procedure. Firstly, the injector characteristics with three different needle vertex angles were found in good agreement with the earlier results of Zhang [1]. Secondly, consistency was obtained between the present wear predictions, previous simulation results [50], and field evidence [10] and [70]. The main findings of this work are as follows.

- Unlike the locations of maximum erosion, the predicted amount of removed material was highly dependent on the choice of the erosion model (Fig. 11a). However, the influence of the wear correlation could be strongly reduced by normalization with a reference condition (Fig. 11b). This indicates that reliable evaluation of the erosion hotspots locations and comparison among different scenarios could be attained even in the lack of case-specific experimental data for calibration.

- Nozzle seat and needle were found the parts of the injector most vulnerable to erosion (Fig. 10), and cutting was identified as the main mechanism of material removal. The predicted integral erosion ratio of the nozzle seat was always higher than that of the needle, but the opening of the injector was likely to affect the wear of the two components in different ways. In fact, whilst the erosion ratio of the nozzle seat did not vary significantly over the entire travel rate, that of the needle increased of about one order of magnitude as the valve was closing (Fig. 11). The enhancement of the needle wear at low valve opening was explained by the higher number of impingements and higher impact velocities (Figs. 12 and 13).

- A decrease of the needle vertex angle from 30° to 25° produced an increase of the erosion of the injector, more evident in the needle (Fig. 14). This was interpreted as a consequence of the higher number of impingements and higher impact angles (Fig. 15). The numerical results also indicated that the effective opening area, which allows unifying the influences of needle vertex angle and opening on the discharge coefficient into a single variable [1], is no longer a similarity parameter for the hydro-abrasive erosion characteristics.

The main limitation of this study is that the employed mathematical model does not account for the synergy between cavitation and silt erosion, which may result in enhanced wear of the needle. Current interest of the authors is the occurrence of cavitation in the injector, with the future goal of developing CFD models capable in predicting the material removal produced by solid particles in the presence of a cavitating flow, thereby improving the accuracy of the needle wear estimates at low openings. To this aim, experimental activities have been also planned to validate the numerical results.

Acknowledgments

The authors would like to acknowledge Hydro Energia s.r.l. for kindly providing the injector geometry.

References

[1] Zhang Z. Pelton Turbines. Berlin: Springer-Verlag; 2016.

[2] Staubli T, Hauser HP. Flow Visualization - A diagnosis Tool for Pelton turbines. In: Proceedings of the International Conference on Hydraulic Measurement and Efficiency IGHEM, Lucerne, Switzerland; 2004.

[3] Unterberger P, Bauer C, Gasch J, Mack R. Studies on the free jet of Pelton nozzles. In: Proceedings of the 16th International Seminar on Hydropower Plants, Wien, Austria; 2010.

[4] Veselý J, Varner M. A case study of upgrading of 62.5 MW Pelton turbine. In: Proceedings of the IAHR International Conference, Praha, Czech Republic; 2001.

[5] Koukouvinis PK, Anagnostopoulos JS, Papantonis, DE. Flow modelling in the injector of a Pelton turbine. In: Proceedings of the 4th Inter SPH European Research Interest Community Workshop SPHERIC '09, Nantes, France; 2009.

[6] Benzon D, Židonis A, Panagiotopoulos A, Aggidis, GA, Anagnostopoulos, JS, Papantonis, DE. Impulse Turbine Injector Design Improvement Using Computational Fluid Dynamics. ASME J Fluids Eng 2015; 137:041106.

[7] Benzon D, Židonis A, Panagiotopoulos A, Aggidis, GA, Anagnostopoulos, JS, Papantonis, DE. Numerical Investigation of the Spear Valve Configuration on the Performance of Pelton and Turgo Turbine Injectors and Runners. ASME J Fluids Eng 2015; 137:111201.

[8] Jo C, Park JH, Kim JW, Shin Y, Chung JT. Jet quality characteristics according to nozzle shape of energy-recovery Pelton turbines in pressure-retarded osmosis. Desalin Water Treat 2016; 57:24626–35.

[9] Zeng C, Xiao Y, Xu W, Wu T, Zhang J, Wang Z, Luo Y. Numerical Analysis of Pelton Nozzle Jet Flow Behavior Considering Elbow Pipe. In: Proceedings of the 28th IAHR symposium on Hydraulic Machinery and Systems IAHR2016, Grenoble, France; 2016.

[10] Bajracharya TR, Acharya B, Joshi CB, Saini RP, Dahlhaug OG. Sand erosion of Pelton turbine nozzles and buckets: A case study of Chilime Hydropower Plant. Wear 2008; 264: 177–84.

[11] Padhi MK, Saini RP. A review on silt erosion in hydro turbines. Ren Sust Energy Rev 2008; 12:1974–87.

[12] Felix D, Albayrak I, Abgottspon A, Boes RM. Hydro-abrasive erosion of hydraulic turbines caused by sediment - a century of research and development. In: Proceedings of the 28th IAHR symposium on Hydraulic Machinery and Systems IAHR2016, Grenoble, France; 2016.

[13] Padhi MK, Saini RP. Effect of size and concentration of silt particles on erosion of Pelton turbine buckets. Energy 2009; 34:1477–83.

[14] Padhi MK, Saini RP. Study of silt erosion on performance of a Pelton turbine. Energy 2011; 36:141–7.

[15] Padhi MK, Saini RP. Study of silt erosion mechanism in Pelton turbine buckets. Energy 2012; 39:286–93.

[16] Abgottspon A, Staubli T, Felix D. Erosion of Pelton buckets and changes in turbine efficiency measured in the HPP Fieschertal. In: Proceedings of the 28th IAHR symposium on Hydraulic Machinery and Systems IAHR2016, Grenoble, France; 2016.

[17] Rai AK, Kumar A, Staubli T, Hydro-abrasive erosion in Pelton buckets: classification and field study. Wear 2017; 392-393:8–20.

[18] Rai AK, Kumar A, Staubli T, Forces acting on particles in a Pelton bucket and similarity considerations for erosion. In: Proceedings of the 28th IAHR symposium on Hydraulic Machinery and Systems IAHR2016, Grenoble, France; 2016.

[19] Thapa B, Chaudhary P, Dahlhaug, OG, Upadhyay P, Study of combined effect of sand erosion and cavitation in hydraulic turbines. In: Proceedings of the International Conference on Small Hydropower, Kandy, Sri Lanka; 2007.

[20] Gohil PP, Saini RP. Coalesced effect of cavitation and silt erosion in hydro-turbines - A review. Ren Sust Energy Rev 2014; 33:280–89.

[21] Morales AM, Pachón IF, Loboguerrero J, Medina JA. Development of a test rig to evaluate abrasive wear on Pelton turbine nozzles. A case study of Chivor Hydropower. Wear 2017; 372:208–15.

[22] Kato C, Yoshimura S. Prediction of the noise from a multi-stage centrifugal pump. In: Proceedings of 2005 ASME Fluids Engineering Division Summer Meeting and Exhibition, Houston, Texas, USA; 2005.

[23] Tan L, Zhu B, Cao S, Wang Y, Wang B. Numerical simulation of unsteady cavitation flow in a centrifugal pump at off–design conditions. Proc IMechE Part C J Mech Eng Sci 2014; 228:1994–2006.

[24] Tan L, Zhu B, Wang Y, Cao S, Gui S. Numerical study on characteristics of unsteady flow in a centrifugal pump volute at partial load condition. Eng Computation 2015; 32:1549–66.

[25] Parsi M, Najmi K, Najafifard F, Hassani S, McLaury BS, Shirazi SA. A comprehensive review of solid particle erosion modeling for oil and gas wells and pipelines applications. J Nat Gas Sci Eng 2014; 21:850–73.

[26] Crowe CT, Schwarzkopf JD, Sommerfeld M, Tsuji Y. Multiphase flows with droplets and particles. Boca Raton, US-FL: CRC Press; 2012.

[27] Bitter JGA, A study of erosion phenomena. Part I. Wear 1963; 6:5–21.

[28] Grant G, Tabakoff W, An experimental investigation of the erosive characteristics of 2024 Aluminium alloy, Technical Report 73-37, Dept Aerospace Engineering, University of Cincinnati, Cincinnati, US–OH; 1973.

[29] Arabnejad H, Development of erosion equations for solid particle and liquid droplet impact, PhD Thesis, University of Tulsa, Tulsa, US–OK; 2015.

[30] Bitter JGA, A study of erosion phenomena. Part II. Wear 1963; 6:169–90.

[31] Neilson JH, Gilchrist A, Erosion by a stream of solid particles. Wear 1968; 11:111–22.

[32] Huang C, Chiovelli S, Minev P, Lui J, Nandakumar K, A comprehensive phenomenological model for erosion of materials in jet flow. Powder Technol 2008; 187:273–9.

[33] Arabnejad H, Mansouri A, Shirazi SA, McLaury BS, Development of mechanistic erosion equation for solid particles. Wear 2015; 332–333:1044–50.

[34] Lyczkowski RW, Bouillard JX, State-of-the-art review of erosion modeling in fluid/solid systems. Prog Energy Comb Sci 2002; 28:543–602.

[35] Leguizamón S, Jahanbakhsh E, Maertens A, Alimirzazadeh S, Avellan F. A multiscale model for sediment impact erosion simulation using the finite volume particle method. Wear 2017; 392:202–12.

[36] Messa GV, Ferrarese G, Malavasi S. A mixed Euler-Euler/Euler-Lagrange approach to erosion prediction. Wear, 2015; 342–43:138–53.

[37] Messa GV, Ingrosso I, Malavasi S. A new methodology for erosion prediction using Eulerian-Eulerian CFD models. In: Proceedings of the ASME Pressure Vessels and Piping Conference, Boston, Massachusetts, USA; 2015

[38] Messa GV, Malavasi S. A CFD-based method for slurry erosion prediction. Wear, 2018; 398–9 (2018) 127–45.

[39] Azimian M, Bart J. Computational analysis of erosion in a radial inflow steam turbine. Eng Fail Anal 2016; 64:26–43.

[40] Campos-Amezcua A, Gallegos-Muñoz A, Romero CA, Mazur-Czerwiec Z, Campos-Amezcua R. Numerical investigation of the solid particle erosion rate in a steam turbine nozzle. Appl Therm Eng 2007; 27:2394-403.

[41] Chitrakar S, Cervantes M, Thapa BS. Fully coupled FSI analysis of Francis turbines exposed to sediment erosion. Int J Fluid Machinery Systems 2014; 7:101–9.

[42] Eltvik M. Sediment Erosion in Francis Turbines. M.Sc. Thesis, Norwegian University of Science and Technology, Trondheim, Norway; 2009.

[43] Li Y, Yan P, Han W. Unsteady Numerical Simulation of Steam-Solid Two-Phase Flow in the Governing Stage of a Steam Turbine. J Therm Sci 2009; 18:313–20.

[44] Ghenaiet A, Tan SC, Elder RL. Prediction of an axial turbomachine performance degradation due to sand ingestion. P I Mech Eng A J Pow 2005; 219:273–87.

[45] Peng G, Wang Z, Xiao Y, Luo Y. Abrasion predictions for Francis turbines based on liquid–solid two–phase fluid simulations. Eng Fail Anal 2013; 33:327–35.

[46] Mazur Z, Palacios LM, Urquiza G. Numerical modeling of gland seal erosion in a geothermal turbine. Geothermics 2004; 33:599–614.

[47] Mazur Z, Campos-Amezcua R, Campos-Amezcua A. Shape modification of an axial flow turbine nozzle to reduce erosion. Int J Num Meth Heat Fluid Flow 2009; 19:242–58.

[48] Roa CV, Muñoz J, Teran LA, Valdes JA, Rodríguez SA, Coronado JJ, Ladino A. Effect of tribometer configuration on the analysis of hydromachinery wear failure. Wear 2015; 332–333:1164–75.

[49] Zeng C, Xiao Y, Zhang J, Ahn S, Wang Z. Numerical analysis of Pelton turbine needle erosion characteristics. J Drain Irrig Mach Eng 2012; 33:407–11. In Chinese.

[50] Zeng C, Xiao Y, Wei Z, Yao Y, Cao L, Wang Z. Pelton turbine Needle erosion prediction based on 3D three- phase flow simulation. IOP Conference Series: Earth and Environmental Science, 2014; 22, 052019.

[51] Loth E, Particles, drops and bubbles: Fluid dynamics and numerical methods, Draft for Cambridge University Press; 2011. Submitted for publication.

[52] Shih TH, Liou WW, Shabbir A, Yang Z, Zhu J. A new $k-\varepsilon$ eddy viscosity model for high Reynolds number turbulent flows, Comput Fluids, 1995; 24:227–38.

[53] Schiller L, Naumann A, A drag coefficient correlation, Z Ver Deutsch Ing, 1935; 77:318–20.

[54] CD-Adapco. STAR CCM+ version 11.02 Documentation, https://stevedocs.cd-adapco.com; 2016.

[55] Messa GV, Malavasi S. The effect of sub-models and parameterizations in the simulation of abrsaive jet impingement tests, Wear, 2017; 370–1:59–72.

[56] Oka YI, Okamura K, Yoshida T. Practical estimation of erosion damage

caused by solid particle impact. Part 1: effects of impact parameters on a predictive equation. Wear, 2005; 259:95–101.

[57] Oka YI, Yoshida T. Practical estimation of erosion damage caused by solid particle impact. Part 2: mechanical properties of materials directly associated with erosion damage. Wear, 2005; 259:102–9.

[58] Oka YI, Matsumura M, Kawabata T. Relationship between surface hardness and erosion damage caused by solid particle impact. Wear, 1993; 162–4:688–95.

[59] Oka YI, Ohnogi H, Hosokawa T, Matsumura M. The impact angle dependence of erosion damage caused by solid particle impact. Wear, 1997; 203–4:573–9.

[60] Zhang Y, Reuterfors EP, McLaury BS, Shirazi SA, Rybicki EF. Comparison of computed and measured particle velocities and erosion in water and air flows. Wear, 2007; 263:330–8.

[61] Okita R, Zhang y, McLaury BS, Shirazi SA. Experimental and Computational Investigations to Evaluate the Effects of Fluid Viscosity and Particle Size on Erosion Damage. J Fluids Eng., 2012; 134:061301.

[62] Nguyen VB, Nguyen QB, Liu ZG, Wan S, Lim CYH, Zhang YW. A combined numerical-experimental study on the effect of surface evolution on the water-sand multiphase flow characteristics and the material erosion behavior. Wear, 2014; 319: 96–109.

[63] Nguyen VB, Nguyen QB, Zhang YW, Lim CYH, Khoo BC. Effect of particle size on erosion characteristics. Wear, 2016; 348–9:126–37.

[64] Det Norske Veritas. Erosive Wear in Piping Systems, Recommended Practice RP O501, https://rules.dnvgl.com/docs/pdf/DNV/codes/docs/2011-01/RP-O501.pdf; 2007.

[65] Haugen K, Kvernvold O, Ronold A, Sandberg R. Sand erosion of wear–resistant materials: Erosion in choke valves. Wear, 1995; 186–7:179–88.

[66] Peng W, Cao X, Numerical prediction of erosion distributions and solid particle trajectories in elbows for gas–solid flow, J. Nat. Gas Sci., 2016; 30:455–70.

[67] Grant T, Tabakoff W. Erosion prediction in turbomachinery resulting from environmental solid particles. J Aircraft, 1975; 12:471-8.

[68] Celik I, Klein M, Freitag M, Janicka J. Assessment measures for URANS/DES/LES: an overview with applications. J Turbul, 2006; 7:48.

[69] Roache PJ. Perspective: A Method for Uniform Reporting of Grid Refinement Studies. J Fluids Eng, 1994; 116:405–13.

[70] Neopane HP, Dahlhaug OG, Cervantes M. Sediment Erosion in Hydraulic Turbines. Global J Res Eng Mech Mech Eng 2011; 9(2):11 pages.

838 **Tables**

Table 1: Number of cells (total and in each domain zone) of the different meshes employed in this study.

	Number of cells			
Mesh ID	Zone 1	Zone 2	Zone 3	Total
M1	7970	662548	201158	871676
M2	11124	1362460	383300	1756884
M3	15047	2810626	597441	3423114
M4	73017	7676673	2487191	10236881

Table 2: Calculation of discretization error. The parameter f is the discharge coefficient, φ_{D_0}, for $\gamma_{\mathrm{n}} = 27.5°$ and $s/D_0 = 0.067$. r is the refinement factor between two grids, calculated making reference to the total number of cells in the domain. The numbers 1 to 3 refer to meshes M1 to M3, respectively. The subscript "ext" stands for the extrapolated solution, which is an estimation of the "exact" one.

r_{12}	1.26
r_{23}	1.25
f_1	0.123
f_2	0.118
f_3	0.117
f_{ext}	0.117
GCI^{23}	0.27%

Figure Captions

Figure 1. Sketch of a Pelton turbine injector.

Figure 2. A solid particle colliding against a surface.

Figure 3. An abrasive jet impingement test.

Figure 4. Half of the computational domain and boundary conditions for (a) the water-air mixture and (b) the parcels.

Figure 5. (a) the different meshing zones; (b) details of mesh M3 close to the needle tip.

Figure 6. Consistency analysis of the integral erosion ratio predictions with respect to the spatial mesh resolution and the number of injected parcels.

Figure 7. VOF solution for $\gamma_{\mathrm{n}} = 27.5°$ and $s/D_0 = 0.459$: (a) mean pressure of the air-water mixture; (b) mean velocity magnitude of the air-water mixture; (c) air volume fraction.

Figure 8. Superimposition of VOF predictions with Zhang's data [1] in terms of: (a) trend of the discharge coefficient as a function of the dimensionless needle stroke; (b) trend of the discharge coefficient as a function of the effective nozzle opening area.

Figure 9. Exemplary particle tracking results for $\gamma_{\mathrm{n}} = 27.5°$ and $s/D_0 = 0.459$: (a) trajectories of 15 representative parcels colored by their local velocity magnitude; (b) the same trajectories of subplot (a) colored by their local Stokes number in logarithmic scale; (c) impact points of 5000 representative parcels colored by the local impact velocity magnitude.

Figure 10. Exemplary results for $\gamma_{\mathrm{n}} = 27.5°$ and $s/D_0 = 0.459$: (a) erosion rate intensity of the nozzle seat; (b) erosion rate intensity of the needle.

Figure 11. Dimensionless needle stroke versus: (a) the integral erosion ratio; (b) the relative integral erosion ratio, where E^* is the integral erosion ratio of the needle at $s/D_0 = 0.45$ (○ = nozzle seat, Oka erosion model; ● = needle, Oka erosion model; △ = nozzle seat, DNV erosion model; ▲ = needle, DNV erosion model).

Figure 12. Erosion of the nozzle seat for $\gamma_{\mathrm{n}} = 27.5°$ and three values of s/D_0: impact points colored by the impact velocity (left column); the same impact points colored by the impact angle (central column); and resulting erosion rate intensity (right column).

Figure 13. The same as Fig. 12 for the needle.

Figure 14. Relative integral erosion ratio versus (a) the dimensionless needle stroke, (b) the effective opening area. The curves are plotted for different values of γ_{n}. E^* is the integral erosion rate of the needle at $s/D_0 = 0.45$ and $\gamma_{\mathrm{n}} = 27.5°$

(Needle data, ♦ : $\gamma_{\rm n} = 25°$; ● : $\gamma_{\rm n} = 27.5°$; ■ : $\gamma_{\rm n} = 30°$. Nozzle seat data, ◊ : $\gamma_{\rm n} = 25°$; ○ : $\gamma_{\rm n} = 27.5°$; □ : $\gamma_{\rm n} = 30°$).

Figure 15. A typical particle trajectory in the space between the needle and the nozzle seat.

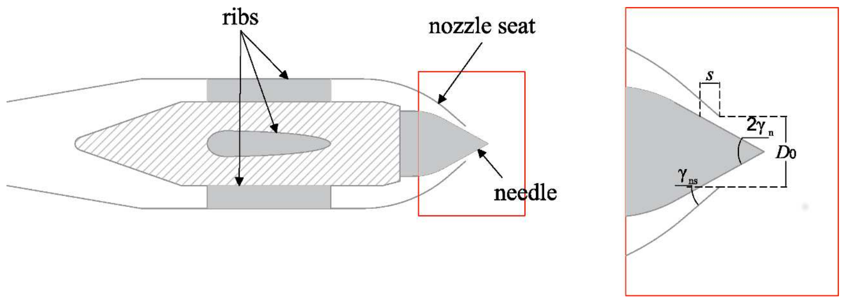
ribs
nozzle seat
needle
s
2γ n
D0
γ ns

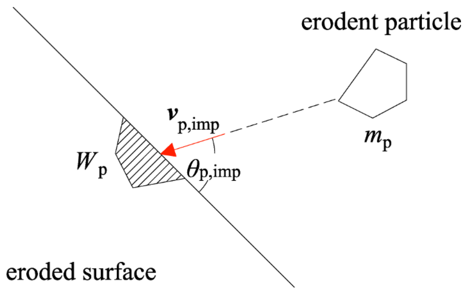

erodent particle
$\boldsymbol{v}_{\mathrm{p,imp}}$
m_{p}
W_{p}
$\theta_{\mathrm{p,imp}}$
eroded surface

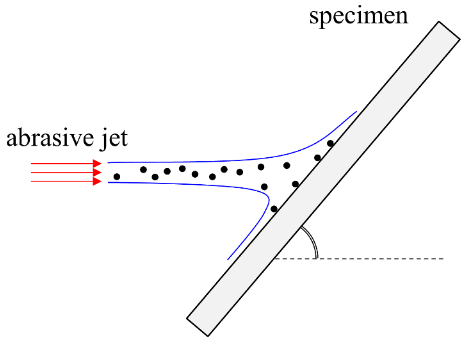
specimen
abrasive jet

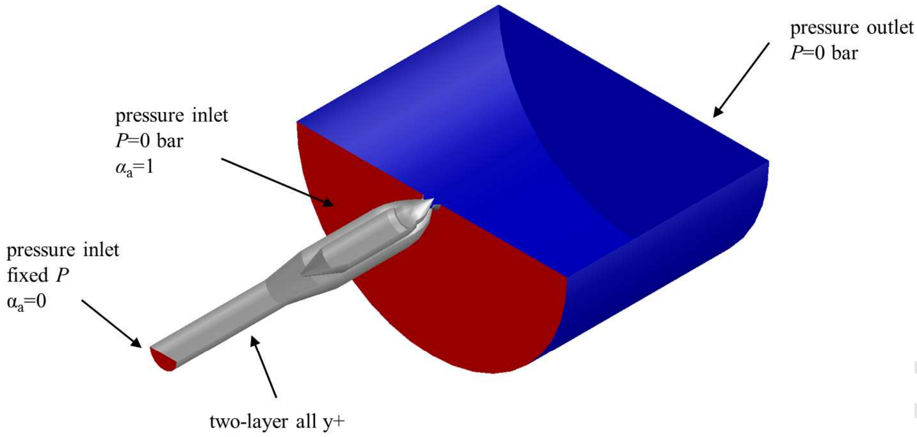
pressure outlet
P=0 bar
pressure inlet
P=0 bar
αa=1
pressure inlet
fixed P
αa=0
two-layer all y+

(a)

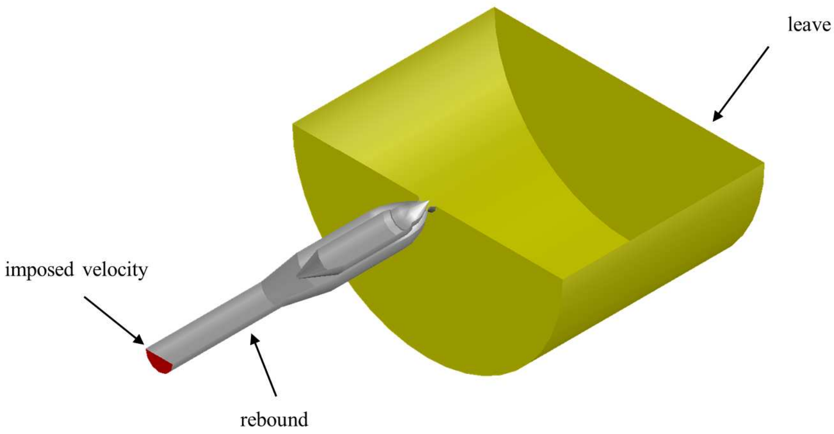
leave
imposed velocity
rebound

(b)

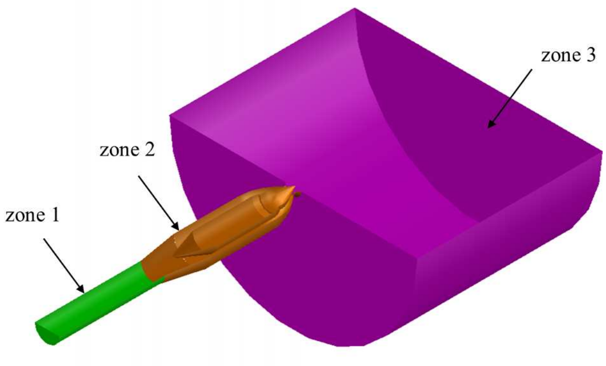

(a)

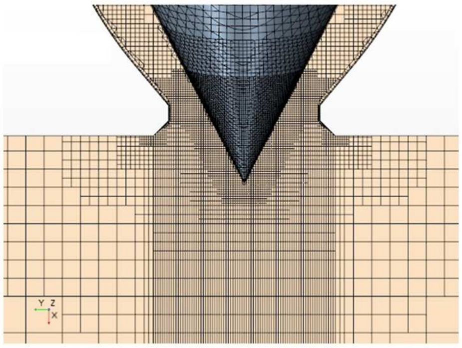

(b)

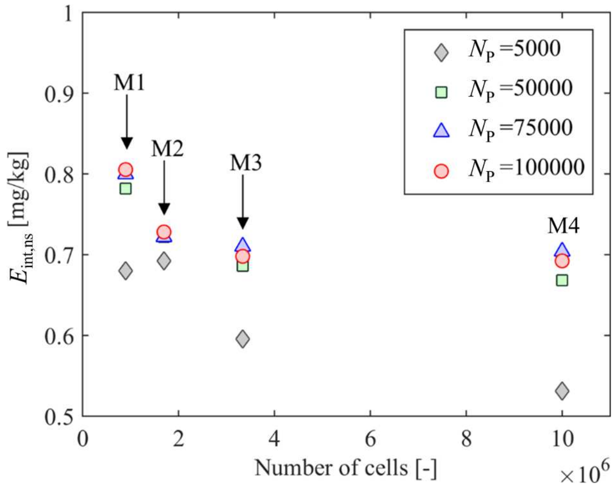

1
0.9
0.8
0.7
0.6
0.5
$E_{int,ns}$ [mg/kg]
0
2
4
6
8
10
Number of cells [-]
$\times 10^6$
M1
M2
M3
M4
N_P =5000
N_P =50000
N_P =75000
N_P =100000

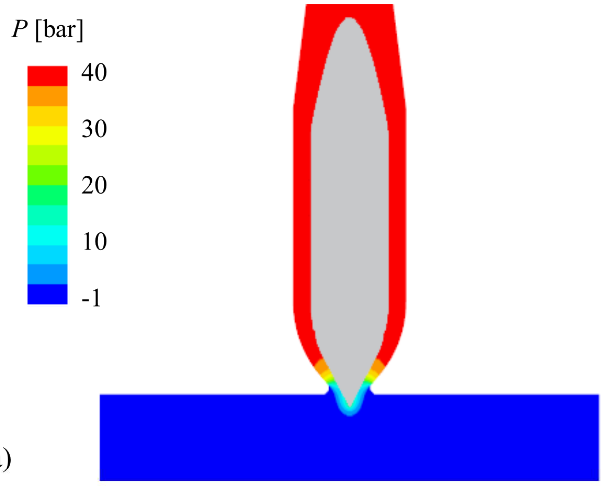

a)

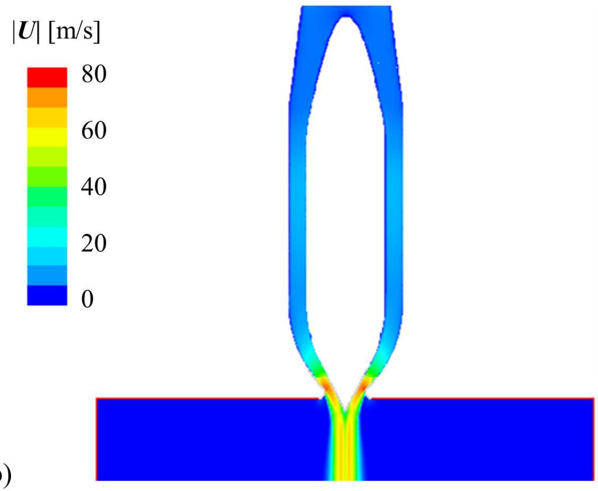

b)

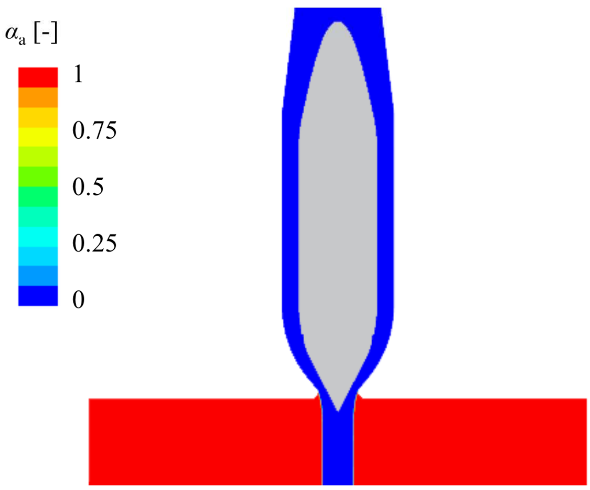

c)

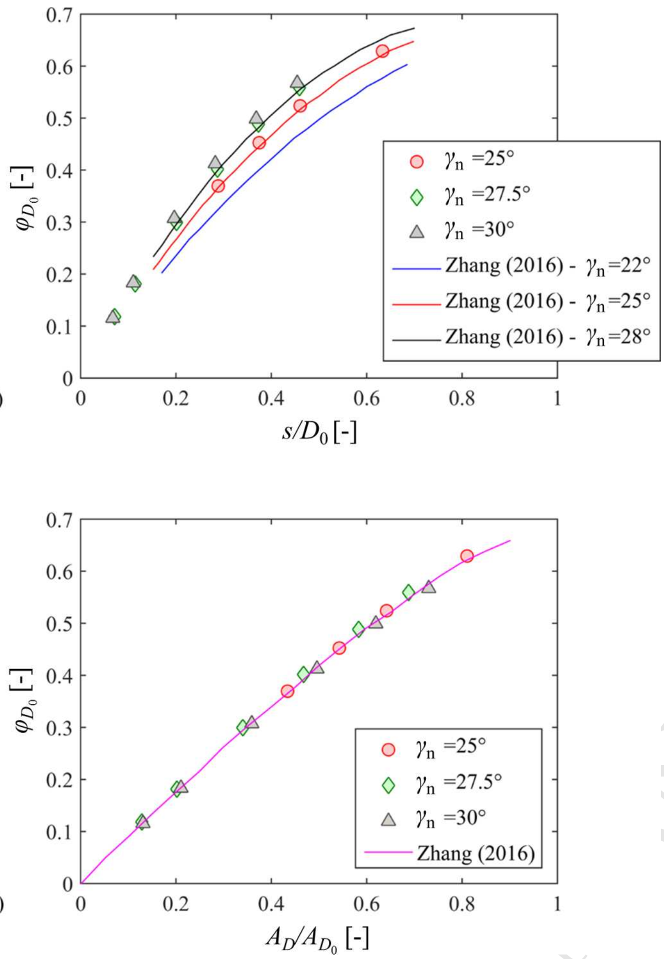
(a)
0.7
0.6
0.5
0.4
0.3
0.2
0.1
0
φ_{D_0} [-]
0
0.2
0.4
0.6
0.8
1
s/D_0 [-]
γ_n =25°
γ_n =27.5°
γ_n =30°
Zhang (2016) - γ_n=22°
Zhang (2016) - γ_n=25°
Zhang (2016) - γ_n=28°
(b)
φ_{D_0} [-]
A_D/A_{D_0} [-]
γ_n =25°
γ_n =27.5°
γ_n =30°
Zhang (2016)

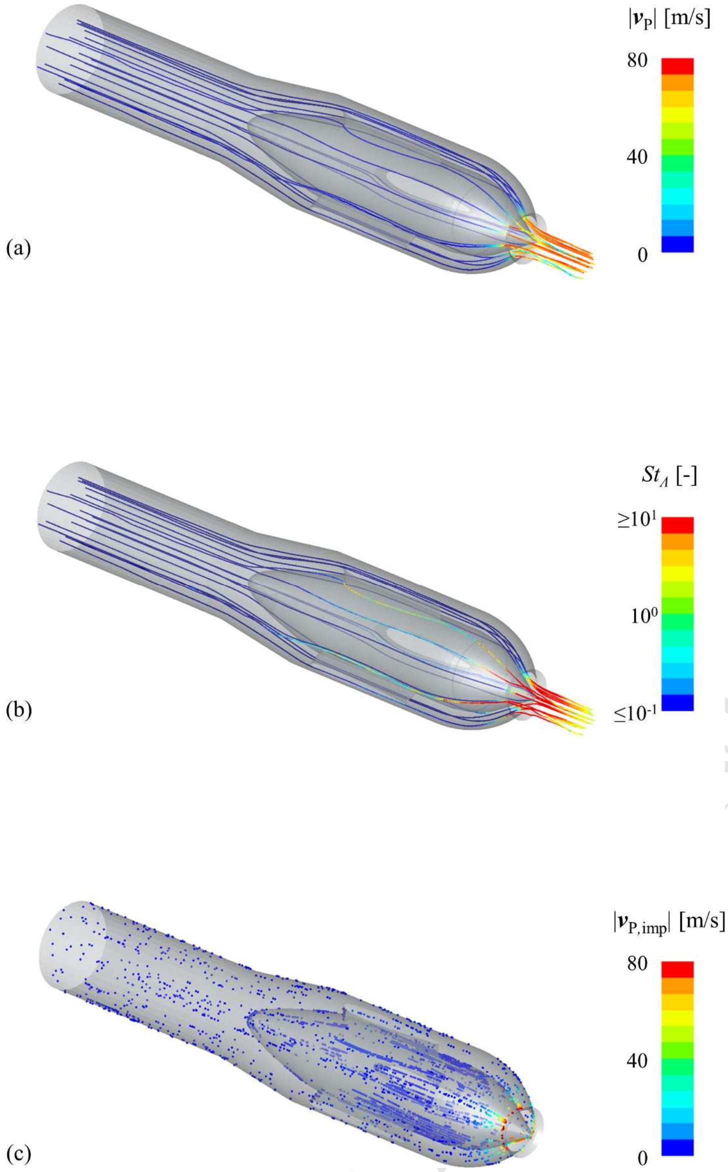
|vP| [m/s]
80
40
0
(a)
StΔ [-]
≥10^1
10^0
≤10^-1
(b)
|vP,imp| [m/s]
80
40
0
(c)

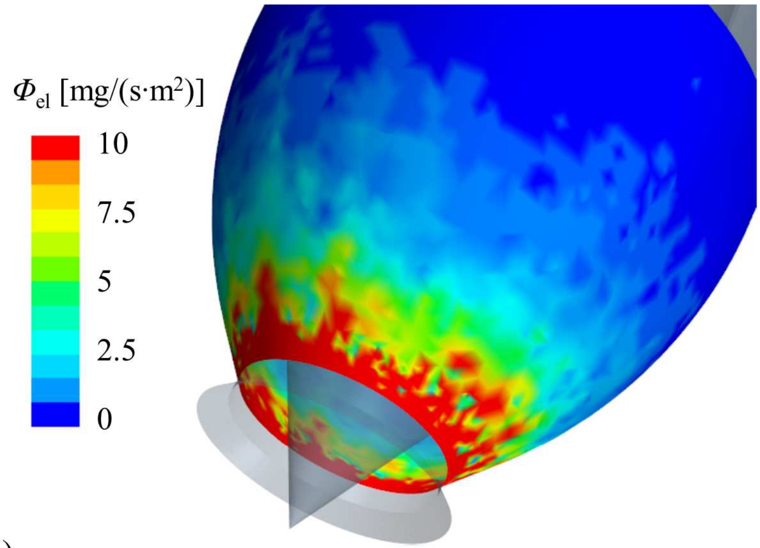

b)

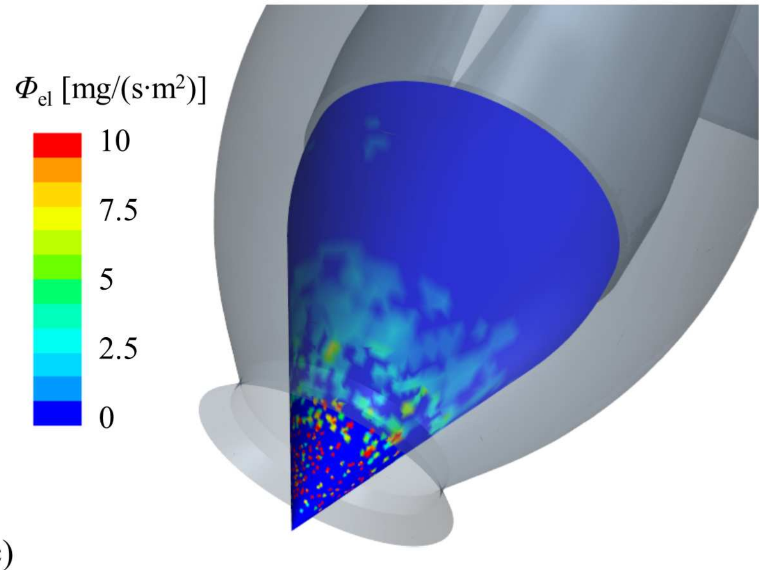

c)

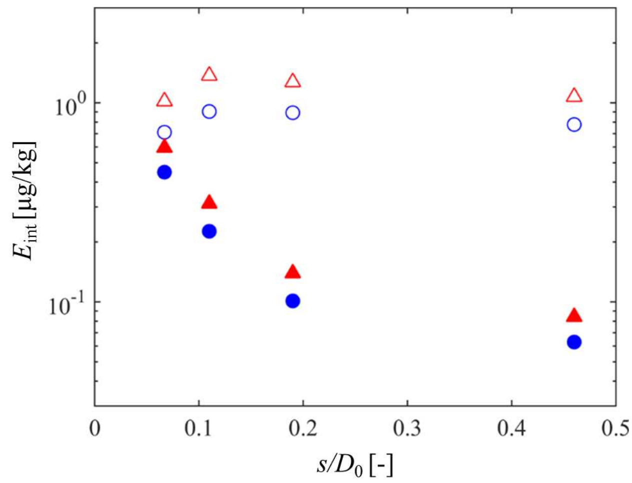

10^0
10^{-1}
E_{int} [µg/kg]
0
0.1
0.2
0.3
0.4
0.5
s/D_0 [-]

(a)

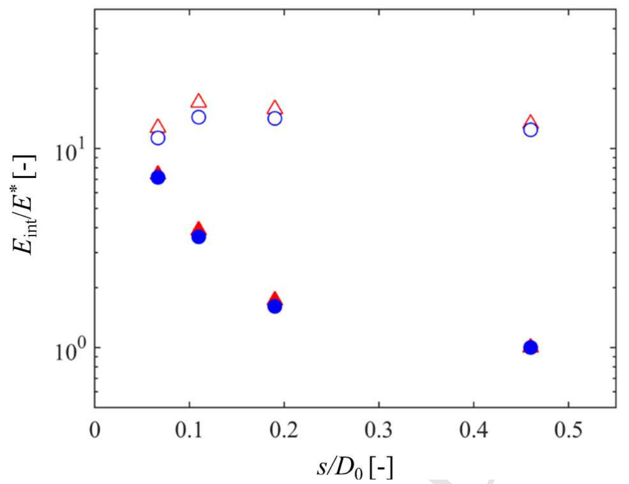

10^1
10^0
E_{int}/E^* [-]
0
0.1
0.2
0.3
0.4
0.5
s/D_0 [-]

(b)

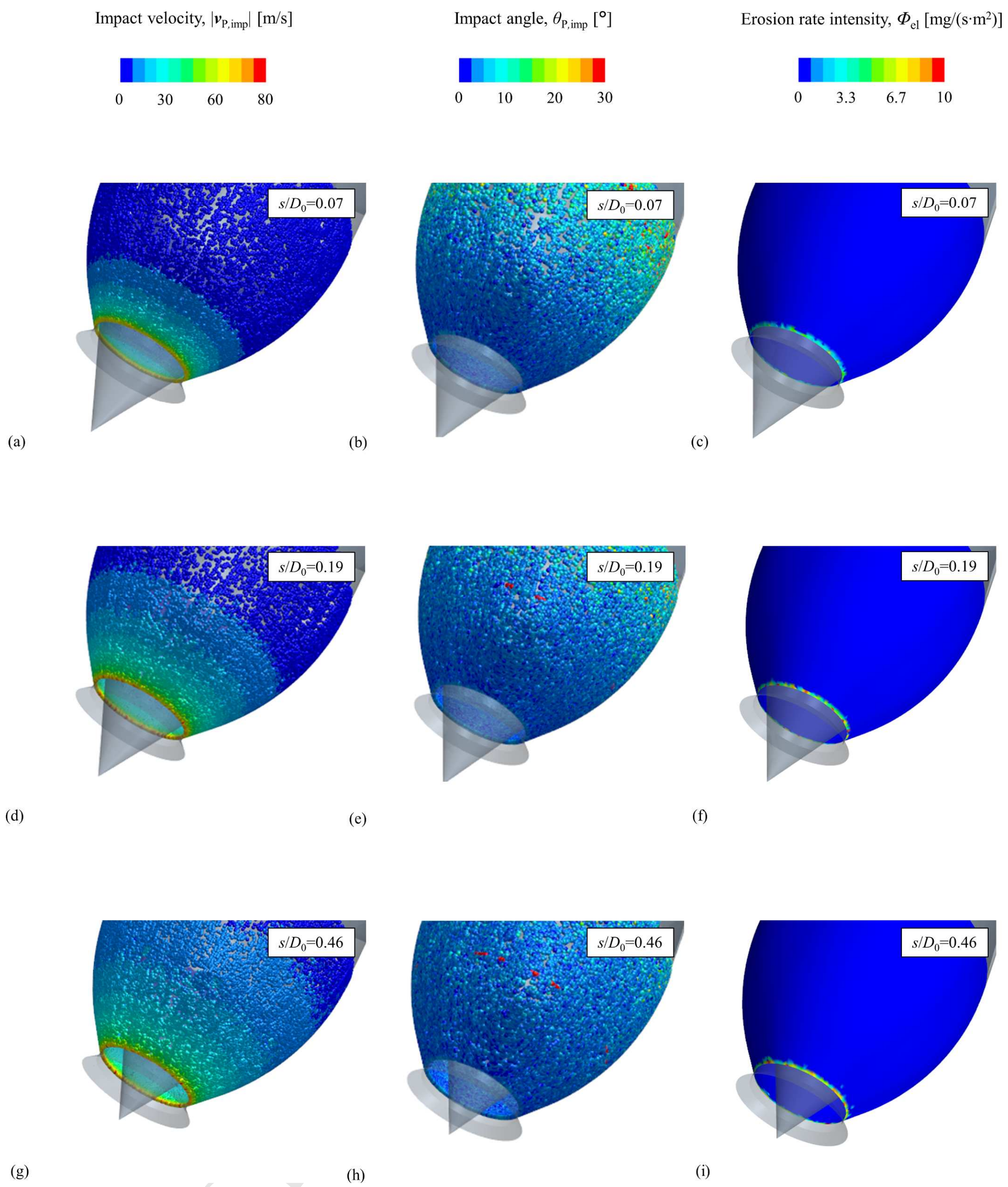

Impact velocity, $|\boldsymbol{v}_{P,imp}|$ [m/s]
0
30
60
80
Impact angle, $\theta_{P,imp}$ [°]
0
10
20
30
Erosion rate intensity, Φ_{el} [mg/(s·m^2)]
0
3.3
6.7
10
s/D_0=0.07
s/D_0=0.07
s/D_0=0.07
(a)
(b)
(c)
s/D_0=0.19
s/D_0=0.19
s/D_0=0.19
(d)
(e)
(f)
s/D_0=0.46
s/D_0=0.46
s/D_0=0.46
(g)
(h)
(i)

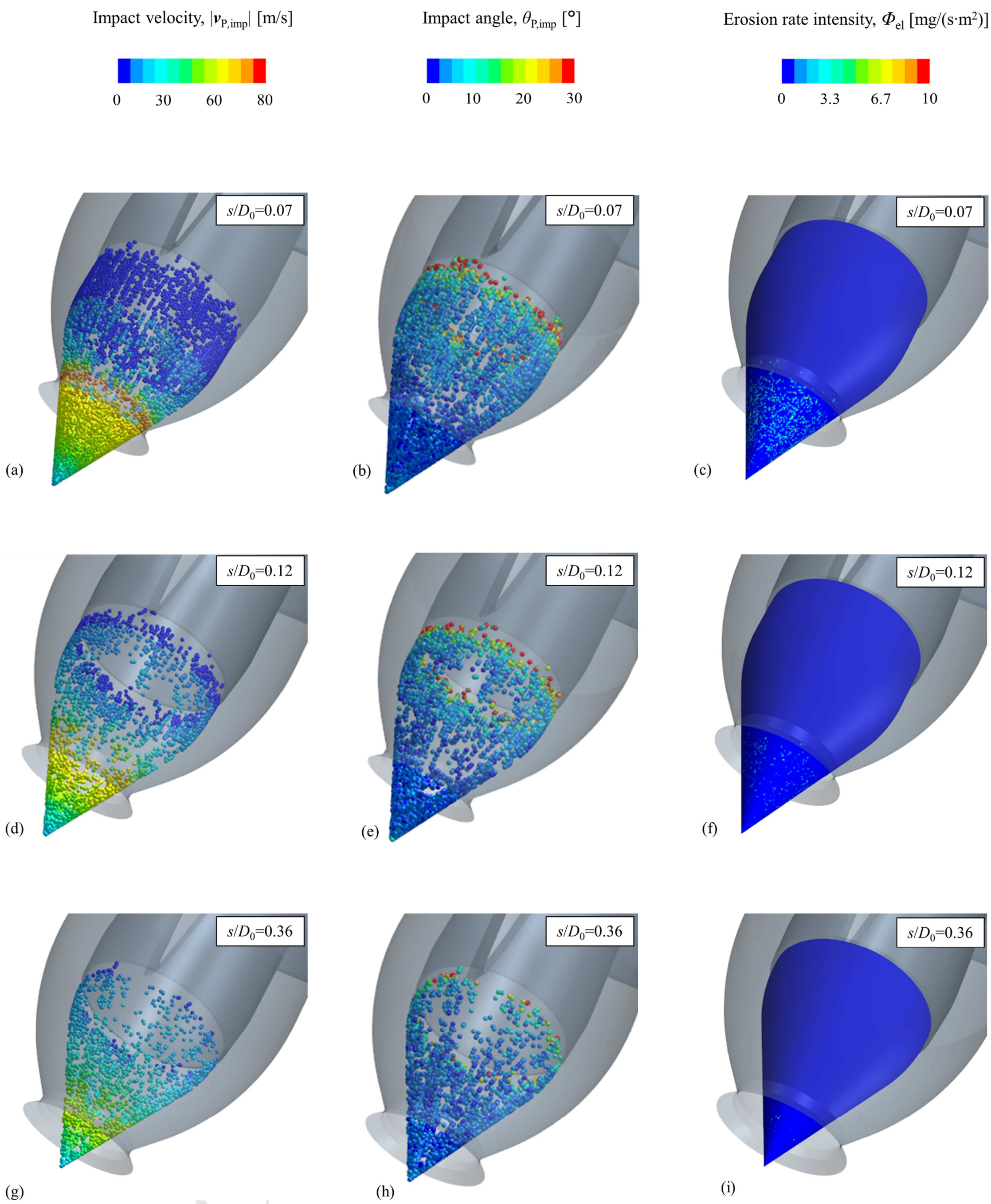

Impact velocity, $|\boldsymbol{v}_{P,imp}|$ [m/s]
0
30
60
80
Impact angle, $\theta_{P,imp}$ [°]
0
10
20
30
Erosion rate intensity, Φ_{el} [mg/(s·m²)]
0
3.3
6.7
10
s/D0=0.07
s/D0=0.12
s/D0=0.36
(a)
(b)
(c)
(d)
(e)
(f)
(g)
(h)
(i)

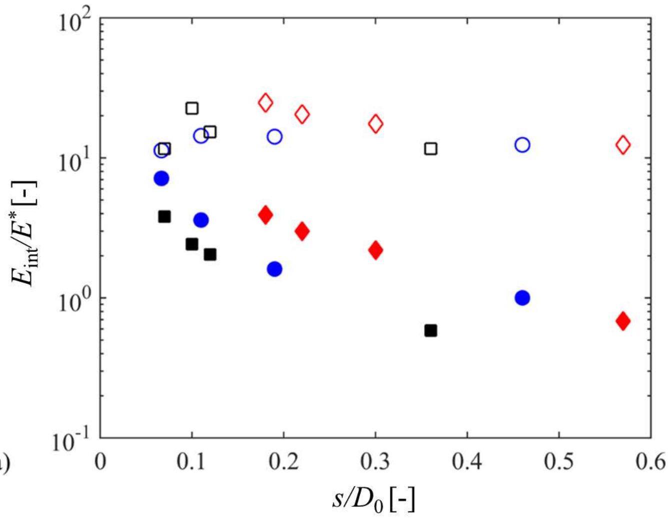

10^2
10^1
10^0
10^{-1}
E_{int}/E^* [-]
0
0.1
0.2
0.3
0.4
0.5
0.6
s/D_0 [-]

(a)

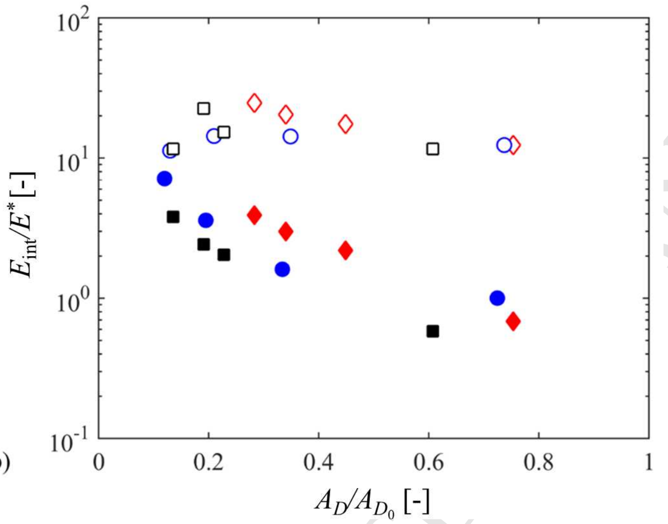

10^2
10^1
10^0
10^{-1}
E_{int}/E^* [-]
0
0.2
0.4
0.6
0.8
1
A_D/A_{D_0} [-]

(b)

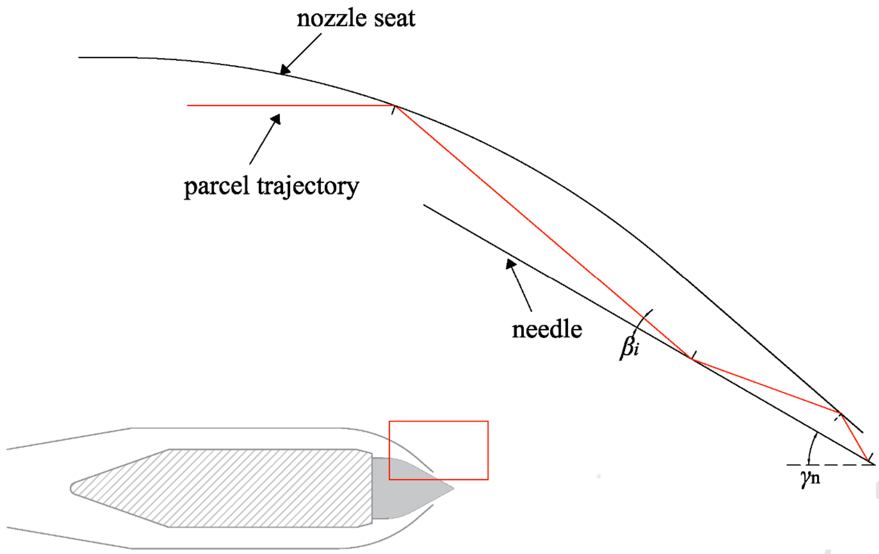
nozzle seat
parcel trajectory
needle
β_i
γ_n

Hydro-abrasive erosion in Pelton turbine injectors: a numerical study.

Gianandrea Vittorio Messa*, Simone Mandelli, Stefano Malavasi
DICA, Politecinco di Milano, Piazza Leonardo da Vinci, 32 20133 Milano, Italy

Highlights

- Particle-laden jets generated by Pelton injector nozzles were numerically simulated
- The regulation characteristics of the injectors were estimated
- The injector components most vulnerable to hydro-abrasive erosion were identified
- The extent of erosion was assessed for different operation and design parameters
- A physical interpretation of the obtained results was provided

*Corresponding author
Email addresses: gianandreavittorio.messa@polimi.it (Gianandrea Vittorio Messa), simone.mandelli@polimi.it (Simone Mandelli), stefano.malavasi@polimi.it (Stefano Malavasi)